

The SunCHECK™ Platform powers Quality Management in radiation therapy.

Scalable to meet the needs of any clinic or network, SunCHECK helps:



Reduce risks



Control costs



Improve treatment quality

Visit sunnuclear.com to learn
how SunCHECK fits into your clinic.



Patient Safety
Starts Here



SUN NUCLEAR
corporation

RESEARCH ARTICLE

MEDICAL PHYSICS

Inferior alveolar canal segmentation based on cone-beam computed tomography

Xueqiong Wei | Yuanjun Wang

School of Medical Instrument and Food Engineering, University of Shanghai for Science and Technology, Shanghai, People's Republic of China

Correspondence

Yuanjun Wang, School of Medical Instrument and Food Engineering, University of Shanghai for Science and Technology, Shanghai 200093, People's Republic of China.
Email: yjusst@126.com

Funding information

Natural Science Foundation of Shanghai, Grant/Award Number: 18ZR1426900; National Natural Science Foundation of China, Grant/Award Number: 61201067

Abstract

Purpose: The shape and position of the inferior alveolar canal (IAC) are analyzed to effectively reduce the risk of iatrogenic injury based on cone-beam computer tomography (CBCT). To assist dental clinicians to make better use of the IAC information, we propose an IAC segmentation method based on CBCT images.

Methods: In this paper, CBCT images are first preprocessed by the Hounsfield unit values clipping and gray normalization. Secondly, based on the multi-plane reconstruction (MPR) and curved surface reconstruction, the curved MPR image sets are generated by the smooth dental arch curve with a sampling distance of 1.00 pixels. Then, the K-means clustering algorithm is used to cluster the texture parameters of the gray level-gradient co-occurrence matrix enhanced by the gradient directions to improve the image contrast of the IAC. Finally, the IAC edges are roughly segmented by the 2D line-tracking method, and smoothed by the fourth-order polynomial to obtain the final segmentation result.

Results: Twenty-one real clinical dental CBCT datasets were used to test the proposed method. The manual segmentation results of two specialized dental clinicians were used as quantitative evaluation criteria. The dice similarity index (DSI), average symmetric surface distance (ASSD), and mean curve distance (MCD) of the left IAC are 0.93 (SD = 0.01), 0.16 mm (SD = 0.05 mm), and 1.59 mm (SD = 0.25 mm), respectively; the DSI, ASSD, and MCD of the right IAC are 0.93 (SD = 0.02), 0.16 mm (SD = 0.05 mm), and 1.60 mm (SD = 0.30 mm), respectively.

Conclusions: The proposed method provides an effective image enhancement and segmentation solution to analyze the shape and position of the IAC. Experimental results show that the relationships between the IAC and other structures can be accurately reflected in the panoramic images without superimposition and geometric distortion, and the smooth edges of the IAC can be segmented.

KEYWORDS

CBCT, gradient enhancement, gray level-gradient co-occurrence matrix, image segmentation, inferior alveolar canal

1 | INTRODUCTION

The inferior alveolar canal (IAC) is a compact bone canal containing the inferior alveolar nerve, the inferior alveolar artery, and the inferior alveolar vein. The IAC starts from the mandibular foramen, enters the mandibular body horizontally forward, and runs along the under-

side of the alveolar bone. The mental nerve, a branch of the inferior alveolar nerve, eventually leaves the IAC through the mental foramen (MF), providing sensation to the anterior aspects of the chin and lower lip, as well as the buccal gingivae of the mandibular anterior and premolar teeth.¹ The anatomical position of the IAC is very close to the root of the tooth. Iatrogenic injury of

inferior alveolar nerves and vessels may occur during root canal treatment, extraction of impacted mandibular third molar (IMTM), and implant treatment due to periapical infection, local anesthesia, overuse of drugs or medical instruments, etc.^{2,3} The anatomical position and direction of the IAC should be taken into account for reducing the incidence of neurosensory disturbance during mandibular invasive surgical procedures such as mandibular osteotomies, fracture repair, and orthognathic surgeries.^{4–6} Therefore, analyzing the shape and position of the IAC has important clinical significance. Cone-beam computer tomography (CBCT) has become one of the important imaging methods for oral and maxillofacial disease diagnosis because of the advantages of high resolution, low radiation dose, and reliable two-dimensional (2D) and three-dimensional (3D) anatomical structure information.^{7–9}

A popular IAC segmentation method based on CBCT is that the MF and mandibular foramen are segmented layer-by-layer in sagittal images. Using matching technology and threshold method to locate the small holes and determine the seed points could improve the segmentation accuracy of the level set method.^{10,11} The influences of the hole shape and image contrast for the IAC segmentation were reduced by low-rank decomposition.^{12,13} To explore the possibility of deep learning technology in the IAC segmentation, Kwak et al.¹⁴ found that the 3D U-Net has certain advantages compared with the 2D SegNet and 2D U-Net. Jaskari et al.¹⁵ showed that the fully convolutional neural network could reduce manual labor in the IAC annotations. However, regardless of the traditional level set method or deep learning technology, those methods are inevitably affected by the shape of the MF and mandibular foramen. The layer-by-layer segmentation also increases the difficulty of experiment.

Another method is based on the curved multi-planar reconstruction (MPR) image set. Due to the scattered distribution of the IAC in the dataset and the low robustness of the 3D line-tracking method, the IAC tracking deviation was still prone to appear in the curved MPR images enhanced by voxel intensity and 3D gradient direction.¹⁶ Although the positioning accuracy of the MF and mandibular foramen was further improved by the 3D panoramic volume rendering and texture analysis, Kim et al.¹⁷ ignored main canal enhancement, which made the cortical layer around the IAC and medulla pattern have a greater impact on the IAC segmentation. Linear objects were automatically extracted according to the shape features of the IAC and then the polynomial function fitting linear objects was usually used to determine the axis of the IAC, which could reduce the experiment time but the IAC is incomplete.^{18,19} Compared with sagittal images, the IAC segmentation based on the curved MPR image set could greatly reduce experimental time, and intuitively obtain the shape and position of the IAC.

Currently, most studies have focused on enhancing the key anatomical structures of the IAC in the curved MPR image set. However, the overall image contrast of the IAC lacks an effective improvement.

In this paper, we propose an IAC segmentation method based on CBCT. First, the curved MPR image set and total average intensity projection (AIP) panoramic image are reconstructed by the MPR and curved surface reconstruction with the sampling distance of 1.00 pixels. Then, we use the K-means clustering algorithm to cluster the texture features of the gray level-gradient co-occurrence matrix (GGCM) of the region of interest (ROI) enhanced by the gradient directions to improve the image contrast of the IAC. Finally, the IAC edges are segmented by the 2D line-tracking method and the 2D line-tracking results are fitted by the fourth-order polynomial to obtain final segmentation results. The proposed method can reconstruct panoramas with good contrast and segment the edges of the IAC. The specific process is shown in Figure 1.

2 | MATERIALS AND METHODS

2.1 | Materials

Each CBCT data was manually segmented by a specialized dental clinician. A total of two professional doctors used ITK-SNAP software to provide the gold standards of 81 CBCT data for quantitative evaluation of experimental results. In this paper, 21 sets of CBCT data were selected for the segmentation experiment of the proposed method. All the datasets were collected from Shanghai Ninth People's Hospital with a resolution of $0.20 \times 0.20 \times 0.20$ mm, the image matrix of each slice is 745×745 pixels, the number of slices in each CBCT volume is 447, and the file format is DICOM. CBCT scans were performed using a K9500 system (Carestream Health Co., United States). The experiments of the proposed method were implemented on Windows 10 desktop computer with Intel(R) Core(TM) i7-9700 CPU (3.00 GHz) and 8 GB memory. The script code was run on MATLAB R2018(a) platform.

Eighty-one curved MPR image sets, with a total of 10 368 images were selected for the experiments of the 2D U-Net and 3D U-Net, as the comparative experiment of the proposed method. The datasets were divided into train: test sets with a ratio of 3:1. All the data were down-sampled and cropped to reduce the amount of data. The data matrix of the 2D U-Net is 256×256 pixels. The data matrix of the 3D U-Net is $128 \times 128 \times 128$ pixels. The experiments of the 2D U-Net and 3D U-Net were implemented on Windows 10 desktop computer with Intel(R) Xeon(R) E5-2683 CPU (2.10 GHz), NVIDIA Quadro P6000 GPU, and 64 GB memory. The script code was run on PyTorch platform.

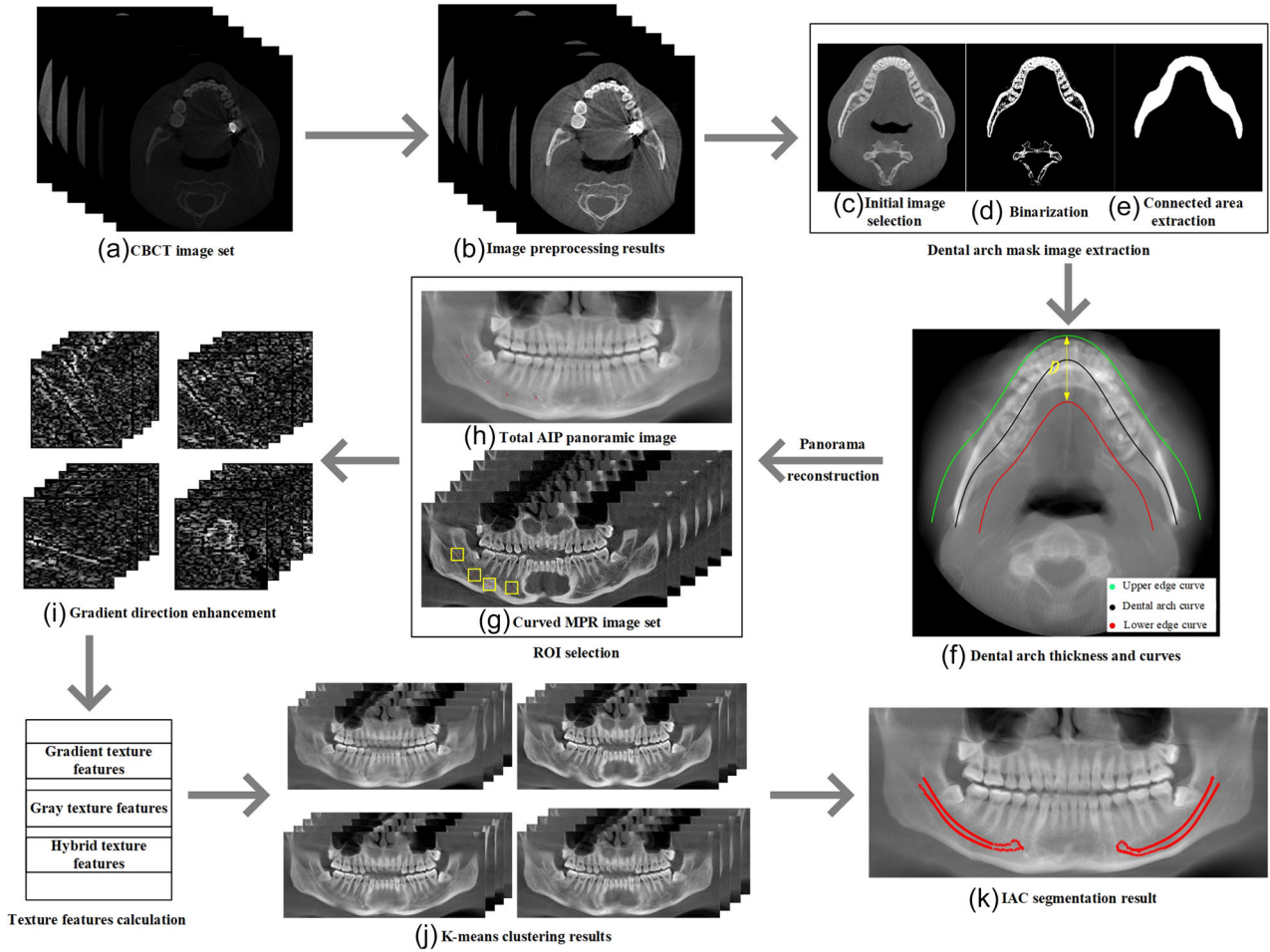


FIGURE 1 Overview of the proposed method for the IAC segmentation

2.2 | Image preprocessing

The Hounsfield unit (HU) value is first clipped during CBCT image preprocessing. The formula for the HU values clipping is as follows:

$$I_1(x, y) = \begin{cases} I(x, y), & I(x, y) < T_1 \\ T_1, & I(x, y) \geq T_1 \end{cases} \quad (1)$$

where (x, y) are the coordinates of the pixel, I is the original image (Figure 1a), I_1 is the resulting image of the HU values clipping, and T_1 is the filtering threshold, while was set to 3000 HU to reduce the impact of ultra-high HU value in this paper.

Then, the gray normalization is used to avoid the nonuniformity of the image pixel brightness.²⁰ The formula for the gray normalization is as follows:

$$I_2(x, y) = \text{round_to_int} \left(\frac{I_1(x, y) - \min}{\max - \min} (2^k - 1) \right) \quad (2)$$

where I_2 is the gray normalization result (Figure 1b), \min is the minimum gray value of I_1 , \max is the maximum gray value of I_1 , and k is the image bits per pixel after normalization, which was set to 8 in this paper. Finally, the grey level of all images is normalized to 0–255.

2.3 | The curved MPR image set reconstruction

The curved MPR image set reconstruction mainly includes three steps: (1) Select a cross-sectional image including teeth and mandible, and extract the dental arch mask image; (2) Calculate the dental arch thickness and dental arch curve; (3) Reconstruct the curved MPR image set and the total AIP panoramic image.

2.4 | Dental arch mask image extraction

To obtain the dental arch mask image, a CBCT image with good continuity between teeth and mandible

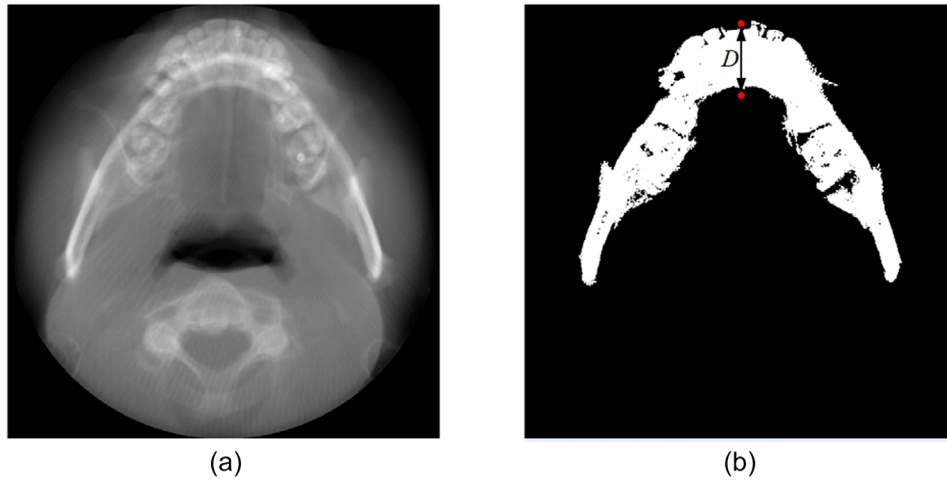


FIGURE 2 (a) The cross-sectional AIP image. (b) The binarized cross-sectional AIP image. The coordinates of the two red dots are (x_1, y_1) and (x_2, y_2) , respectively. The Euclidean distance between the two red dots is the dental arch thickness D

needs to be selected, generally the mandibular dental neck image. Since the mandibular dental neck images approximately distribute at 1/3 of the CBCT volume, we took the 149th CBCT image as the initial image (Figure 1c). The initial image needs to include the basic shape of the mandible with smooth edges to ensure the initial dental arch curve has good continuity.

The initial image is first binarized (Figure 1d), and then the largest connected area is extracted and filled to obtain the dental arch mask image (Figure 1e).

2.5 | Dental arch curve determination

The dental arch thickness D is the maximum width of the tooth and mandible region in the cross-sectional AIP image (Figure 2a), which is the number of slices in the curved MPR image set volume. The formula for the dental arch thickness D is as follows:

$$D = \sqrt{(x_2 - x_1)^2 + (y_2 - y_1)^2} \quad (3)$$

where (x_1, y_1) and (x_2, y_2) are the coordinates of the upper and lower edge points of the maximum width region, respectively. They are manually selected in the binarized cross-sectional AIP image (Figure 2b). Generally, the dental arch thickness D is 100 to 140 pixels.

The initial dental arch curve is often extracted by the morphological skeletonization. In this paper, the skeleton extraction and deburring were implemented based on the MATLAB function—`bwmorph`.^{19,21,22}

The dental arch curve needs to be smooth and continuously differentiable, so the initial dental arch curve needs to be fitted. The sampling points with the same distances could be obtained by the equidistant sampling. In this paper, the initial dental arch curve was fitted by

the sixth-order polynomial. Because of the input images with isotropic pixel sizes, the fitting result was sampled equidistantly with the sampling distance of 1.00 pixels to obtain the panoramic images with isotropic resolution. The final dental arch curve is shown as the black curve in Figure 1f.

The initial coordinate points of the upper and lower edge curves are calculated by formula 4, and then the edge curves are fitted by the sixth-order polynomial. The final upper and lower edge curves are shown as the green and red curves in Figure 1f.

$$\begin{cases} x_U = x + \frac{(D/2)}{\sqrt{1 + (dy/dx)^2}} \\ y_U = y - \frac{(dy/dx) \times (D/2)}{\sqrt{1 + (dy/dx)^2}} \\ x_L = x - \frac{(D/2)}{\sqrt{1 + (dy/dx)^2}} \\ y_L = y + \frac{(dy/dx) \times (D/2)}{\sqrt{1 + (dy/dx)^2}} \end{cases} \quad (4)$$

where (x, y) is the sampling point of the dental arch curve, (x_U, y_U) and (x_L, y_L) are the initial coordinate points of the upper and lower edge curves, respectively. (dy/dx) is the derivative value of the dental arch curve, D is the dental arch thickness.

2.6 | Image reconstruction

The two-line interpolation is used to calculate D offset curves of the normal vector direction of the dental arch curve. Then, the curved MPR image (Figure 1g) of

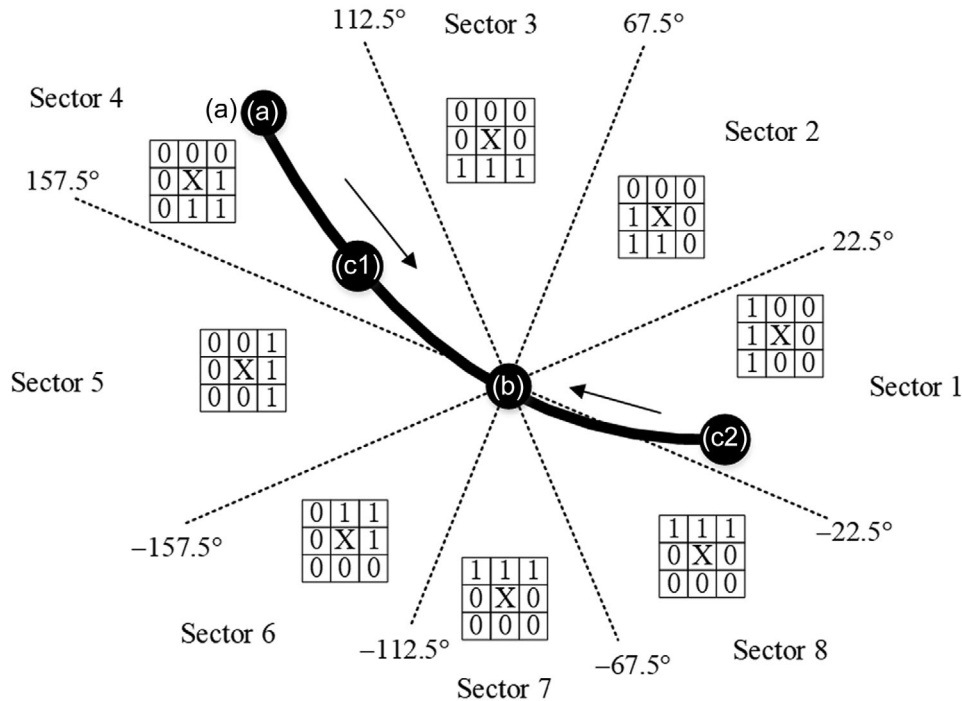


FIGURE 3 Schematic diagram of the 2D line tracking with eight angle ranges and domain templates. A is the tracking start point. B is the endpoint. C₁ and C₂ are the segment points. X denotes the current pixel. The black arrows indicate the tracking directions

each offset curve is reconstructed based on the MPR and curved surface reconstruction.^{22–24} The number of slices in each curved MPR image set volume is the value of the dental arch thickness D . The width and height of each curved MPR image are the length of the dental arch curve and the volume of CBCT, respectively. Finally, the total AIP panoramic image (Figure 1h) generated based on the curved MPR image set helps to visually analyze the relationship of various anatomic structures.

2.7 | IAC enhancement

The contrast of the IAC is not only affected by the cortical layer and medulla pattern, but also by the distribution characteristics of the IAC. The left and right of the IAC are often symmetrically distributed and the various parts of the IAC are distributed in different layers, so the superposition of all layers could affect the sharpness of the IAC edges. Therefore, we propose an effective IAC enhancement method to improve the contrast of the IAC.

2.8 | ROI selection

The images containing IAC information are concentrated in the middle part of the curved MPR image set, roughly distributed in $[D/4, 3D/4]$. In this paper, the first quarter and the last quarter number of layers in the curved MPR image set volume were sieved. The

intermediate layers (50–70 layers) of the dataset were selected for the subsequent experiment, and since the size of each voxel is $0.20 \times 0.20 \times 0.20$ mm, the physical dimension is 10.00–14.00 mm.

According to the basic shape and direction of the IAC, four center points of the ROI on the same side of the IAC were selected manually in the total AIP panoramic image to generate ROI sets, which are distributed in the MF, as well as the front, middle, and back of the canal (Figure 1h red dots). Each ROI is a square area of 61×61 pixels (Figure 1g yellow areas). According to the symmetry of the IAC, generally enhancing the ROI sets on one side could strengthen both sides at the same time. In addition, the IAC is a continuous narrow and long canal. As long as the center points of the ROI are selected in different parts of the IAC, the K-means clustering results are less affected by the difference in the center points.

2.9 | Gradient direction enhancement

To obtain the GGCM of the ROI, the gradient of the ROI needs to be calculated first. However, because the IAC is a non-empty canal, there is a lot of low gray-level noise in the gradient images. According to the distribution characteristics of the IAC, it is divided into eight sectors¹⁶ (Figure 3). Each sector has a specific angle range and domain template. The gradient direction enhancement method is summarized as follows:

Step 1: Steps 2–5 are performed for each image of ROI set to calculate the gradient direction enhancement set G (Figure 1i). $R(x, y)$ is current image, where $x = 1, 2, \dots, M$, $y = 1, 2, \dots, N$; M and N are the number of the image rows and columns, respectively.

Step 2: The weighted average gradient $g(x, y)$ of $R(x, y)$ is used for calculating of the gradient direction $\theta(x, y)$ and the largest pixel point $m(x_{\max}, y_{\max})$. The formula for the weighted average gradient $g(x, y)$ of $R(x, y)$ is as follows:

$$\begin{aligned} g_x(x, y) &= R(x+1, y-1) + 2R(x+1, y) \\ &\quad + R(x+1, y+1) - R(x-1, y-1) \\ &\quad - 2R(x-1, y) - R(x-1, y+1) \\ g_y(x, y) &= R(x-1, y+1) + 2R(x, y+1) \\ &\quad + R(x+1, y+1) - R(x-1, y+1) \\ &\quad - 2R(x, y-1) - R(x+1, y-1) \\ g(x, y) &= \sqrt{g_x^2 + g_y^2} \end{aligned} \quad (5)$$

Step 3: The formula for the gradient direction $\theta(x, y)$ of $R(x, y)$ is as follows:

$$\theta(x, y) = \arctan \left[-\frac{g_x(x, y)}{g_y(x, y)} \right] \quad (6)$$

Step 4: According to $\theta(x, y)$, $g(x, y)$ is determined to fall into which sector of Figure 3.

Step 5: According to the domain template of each sector, the largest pixel point $m(x_{\max}, y_{\max})$ of the weighted average gradient $g(x, y)$ is calculated and recorded into G , where (x_{\max}, y_{\max}) is the coordinate of the largest pixel in the domain template.

2.10 | GGCM and texture features calculation

The GGCM not only reflects the distribution law of gray level and gradient, but also reflects the spatial relationship between each pixel in the domain. By clustering the texture features of the GGCM, it is possible to detect the layers with the IAC edge, reduce useless information, and enhance the IAC contrast.

The GGCM was calculated from the ROI set R and the gradient direction enhancement set G .^{25,26} To describe the gradient features and gray features more accurately, we divided texture features into three categories: (1) gradient texture features; (2) gray texture features; (3) hybrid texture features. The texture features of the GGCM are shown in Appendix A.

2.11 | K-means clustering algorithm

Three categories of texture features are respectively clustered by the K-means clustering algorithm to more accurately classify the curved MPR image set, and then the clustering results are integrated and clustered again to obtain the final classification results.

In this paper, the kmeans function of MATLAB was used to implement the K-means clustering algorithm. In the function, the number of repetitions is one; the type of distance is "sqeuclidean"; the number of iterations is 100; the type of centroid initialization is "plus." Because the ROI set contains roughly four types of images: (1) The IAC edge images; (2) The mandibular edge images distributed at a certain angle; (3) The mandibular images with uniform low gray-level pixels; (4) The mandibular images with uniform high gray-level pixels, the texture features can be divided into four clusters each time. Finally, the clustering results are reconstructed by the AIP to obtain the new panoramas (Figure 1j).

2.12 | IAC segmentation

The IAC boundaries are segmented by the 2D line-tracking method. First, the starting point A is determined to fall into which sector of Figure 3, and the largest pixel point p of the domain template is calculated as the next start point, until the tracking endpoint B .¹⁶ To avoid tracking deviations and ensure the integrity of the segmentation results, multiple segment points such as point C_l ($l = 1, 2, 3, \dots$) can be added for segment tracking.

In this paper, we manually selected the tracking start point A , endpoint B , and segment point C_l in the new panoramas to roughly segment the IAC edges by the 2D line-tracking method. The point A is generally selected at the upper end of the IAC, at the edge of the mandibular foramen; the point B is selected at the turning points between the main canal and the MF; the point C_l could be set at the edge of the middle canal and the MF. However, the rough segmentation results were affected by the uneven gray-level distribution of the canal, which was easy to generate tracking deviations and burrs. To obtain smooth edges, the edges with more burrs could be fitted by the fourth-order polynomial. Finally, the segmentation results are displayed in the total AIP panorama image to analyze the relationship between the IAC and other structures (Figure 1k).

3 | RESULTS

3.1 | Qualitative evaluation

Figure 4 shows the three sets of the dental arch curves and panoramas. Figure 4a–c shows the fitting results of the dental arch curves, in which the dental arch

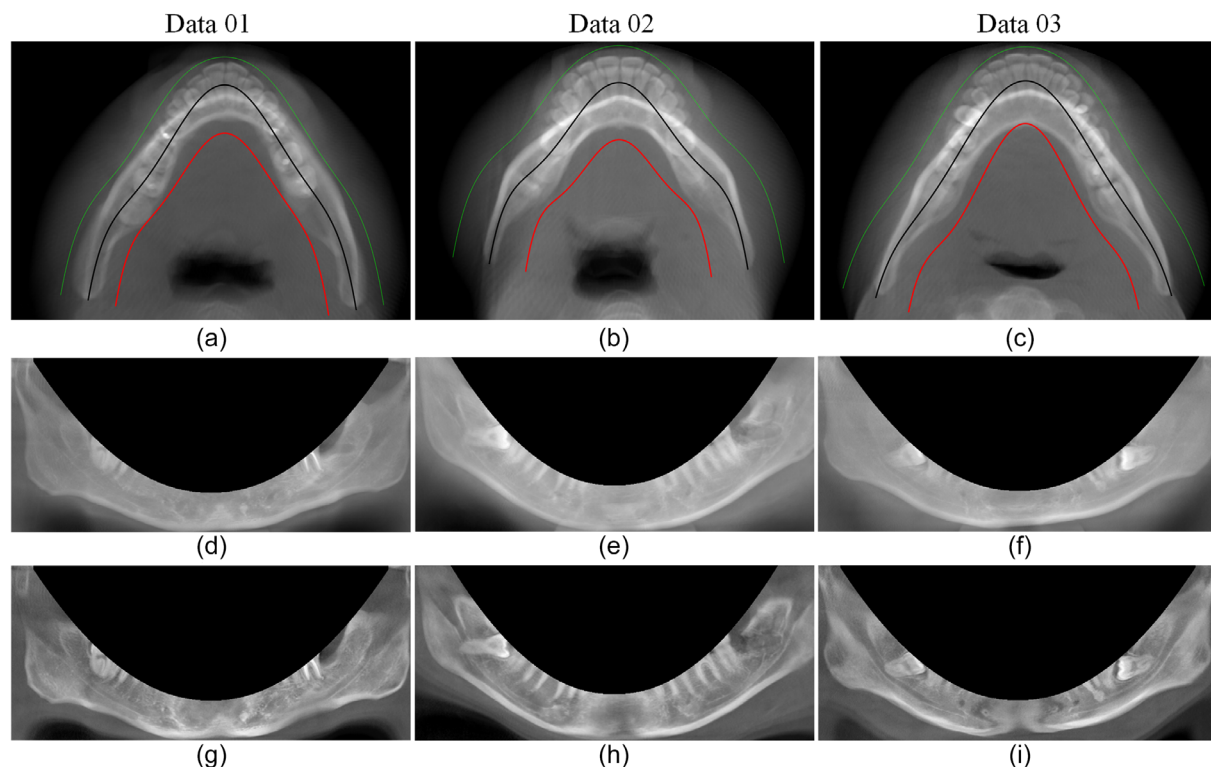


FIGURE 4 Reconstruction results of the three CBCT sets. (a–c) The fitting results of the curves. The black curves are the dental arch curves; the green and red curves are the upper and lower edge curves, respectively. (d–f) The total AIP panorama images. (g–i) The new panoramas with the proposed method

thicknesses D of the three data are 105, 139, and 127 pixels, respectively. The dental arch curves are smooth and continuous; the curve shapes are consistent with the shapes of the mandible. The upper and lower edge curves are close to the edges of the entire tooth and mandible area to ensure the integrity of the total AIP panorama images. To better display the enhanced results, the tooth areas are removed in Figure 4d–i. Figure 4d–f shows the total AIP panorama images. Affected by metal artifacts and image superposition, the IACs have extremely low contrast and the edges are very blurred in the total AIP panorama images. Figure 4g–i shows the new panoramas enhanced by the proposed method. Compared with the total AIP panorama images, the new panoramas have a higher contrast in the IAC. The IAC edges on both sides are clearly visible and the positions of MF are obvious.

Figure 5 shows the gradient direction enhancement results. The edges of the mandible and IAC have similar gradient information, especially when the IAC is close to the edges of the mandible. If the texture features calculated in the original ROI are directly clustered, incorrect clustering results will be obtained. However, since the IAC is a non-hollow canal containing soft tissue, after the gradient direction enhancement, its edges are sharper and have different gradient information compared with the other three types of images.

Since the accuracy of the K-means clustering algorithm is also affected by the amount of data, to make full use of the 15 texture parameters of the GGCM with the gradient direction enhancement, we first divided them into three categories for initial clustering, and then integrated the clustering results to cluster again to obtain the final classification results. After clustering twice, we can effectively extract the layers with the same attributes.

Figure 6 shows the panoramic images under different enhancement methods. Figure 6a is the total AIP panorama image without any enhancement, and Figure 6e is the final new panorama enhanced by the proposed method. Compared with Figure 6a without any enhancement, the image contrast enhanced by one or more ways is improved to a certain extent, the IAC edges are roughly visible and Figure 6e enhanced by the proposed method has the best image contrast.

Figure 7 shows the IAC segmentation results. The 2D line-tracking method is based on the domain templates to detect the IAC edges. When the cortex layer around the IAC is thin, the medulla pattern is unclear, or the IAC is close to the edges of the mandible, the 2D line-tracking method will cause segmentation deviations (The blue IACs in Figure 7). Since the IAC has the parabolic distribution characteristic, segmentation results with burrs are fitted by the fourth-order polynomial, which can effectively further reduce the

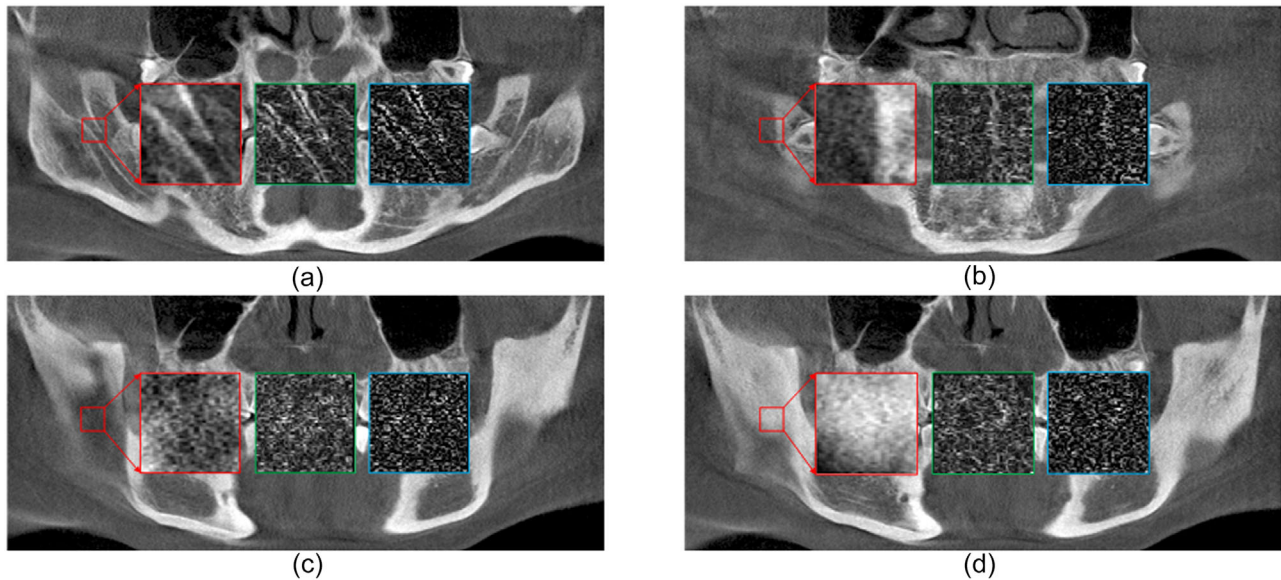


FIGURE 5 Four types of ROI. The smaller red border images indicate the position of ROIs in the panoramas. The larger red border images denote the ROIs of 61×61 pixels. The green border images are the gradient images and the blue border images are the gradient direction enhanced images. (a) The IAC edges. (b) The mandibular edges. (c) Uniform low gray-level pixels. (d) Uniform high gray-level pixels

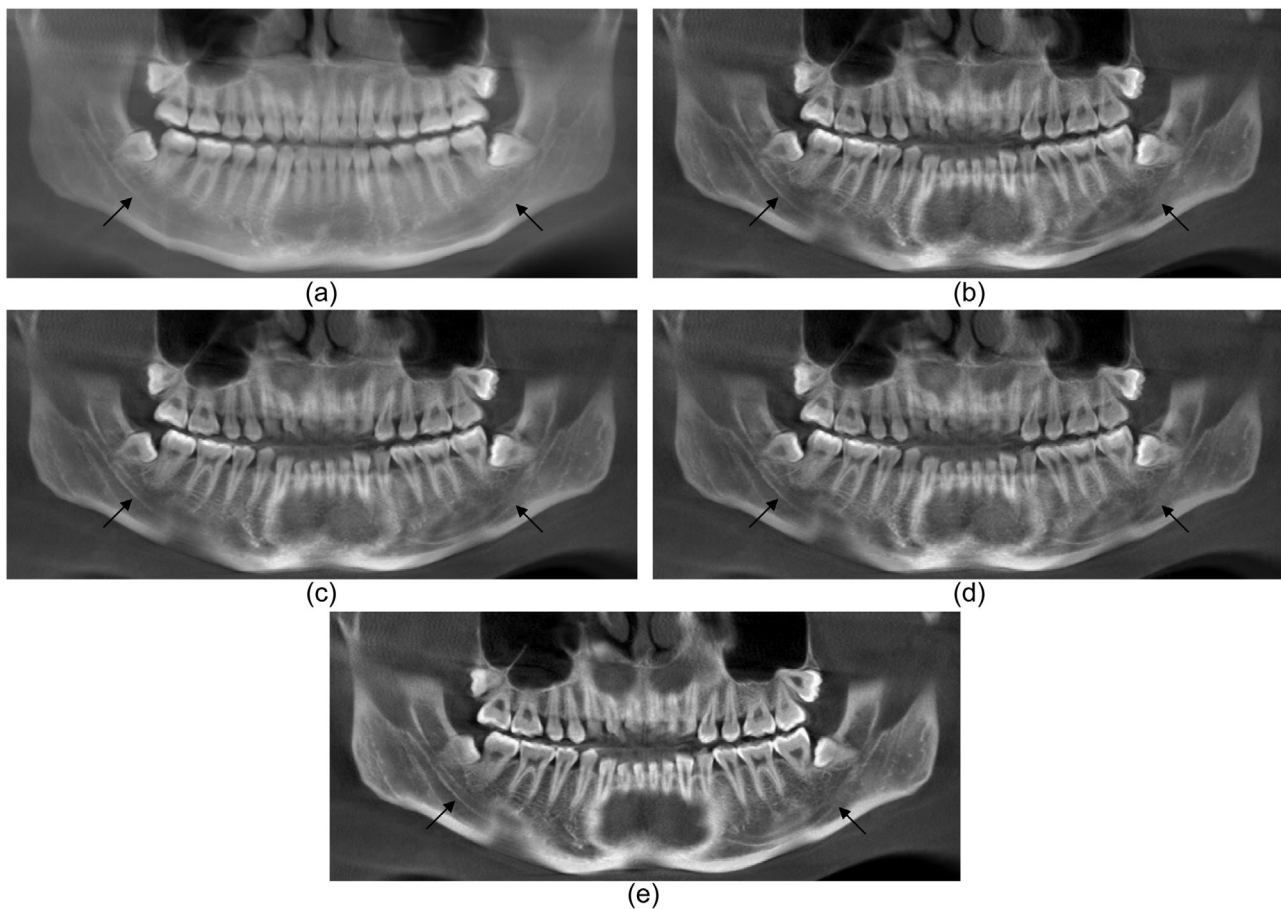


FIGURE 6 Comparison of panoramic images under different enhancement methods. The black arrows point to the IAC. (a) The total AIP panorama image without any enhancement. (b) The panorama with K-means clustering algorithm. (c) The panorama with gradient direction enhancement and K-means clustering algorithm. (d) The panorama with texture features classification and K-means clustering algorithm. (e) The final new panorama with the proposed method

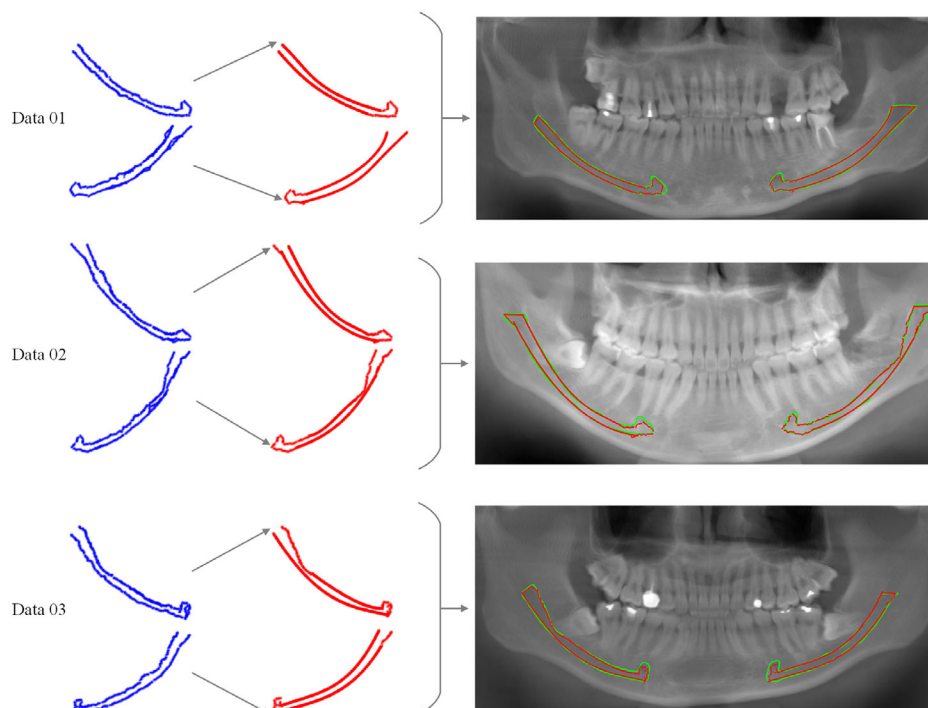


FIGURE 7 Segmentation results of the IAC. The blue IACs are the 2D line-tracking results. The red IACs are the fitting results based on the fourth-order polynomial. The green IACs are the doctor segmentation results. The last column total AIP panorama images show the comparison between the segmentation results of the proposed method and doctors

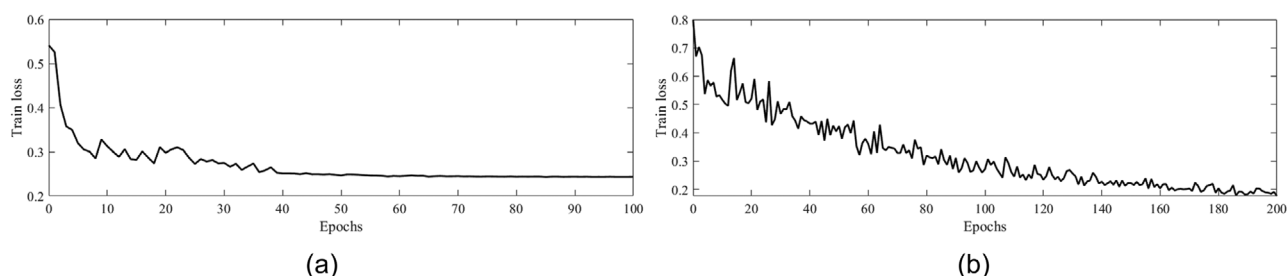


FIGURE 8 Training progress of each network. (a) Training loss of 2D U-Net with 100 epochs. (b) Training loss of 3D U-Net with 200 epochs

tracking deviations (The red IACs in Figure 7). The last column images of Figure 7 are the comparison between the segmentation results of our experiments and doctors. It shows that the proposed method can accurately segment the smooth IAC edges, identify the intersection of the IMTM and IAC, locate basically the MF.

Currently, some studies have initially explored the feasibility of deep learning technology to segment the IAC.^{14,15} Based on the curved MPR image set, this paper used the 2D U-Net and 3D U-Net for comparative experiments. The 2D U-Net model was trained for 100 epochs, and the 3D U-Net model was trained for 200 epochs. All of them used Adam optimizer with a learning rate of 0.001, a momentum of 0.9, the Dice loss function, the ReLU function, and the batch size of 8 for the 2D/3D U-Net. As shown in Figure 8, the training loss of 2D U-Net

converges to 0.25 within 100 epochs, and the training loss of 3D U-Net converges to 0.2 within 200 epochs.

Since the left and right sides of the IAC have a certain symmetry, Figure 9 shows the comparison of the proposed method, 2D U-Net, and 3D U-Net for the left IAC segmentation results. The red IACs are the segmentation result, and the green IACs are the doctor segmentation results. The cortical layer around the IAC is generally ambiguous, and there is no obvious boundary between the IAC and the surrounding tissues. Therefore, the over-segmentation or under-segmentation seriously appeared in the results of the 2D U-Net and 3D U-Net. In some bad cases, the IAC region cannot even be identified. The proposed method in this paper enhanced the image contrast of the IAC in the curved MPR image set, and the edges of the IAC were sharpened to a

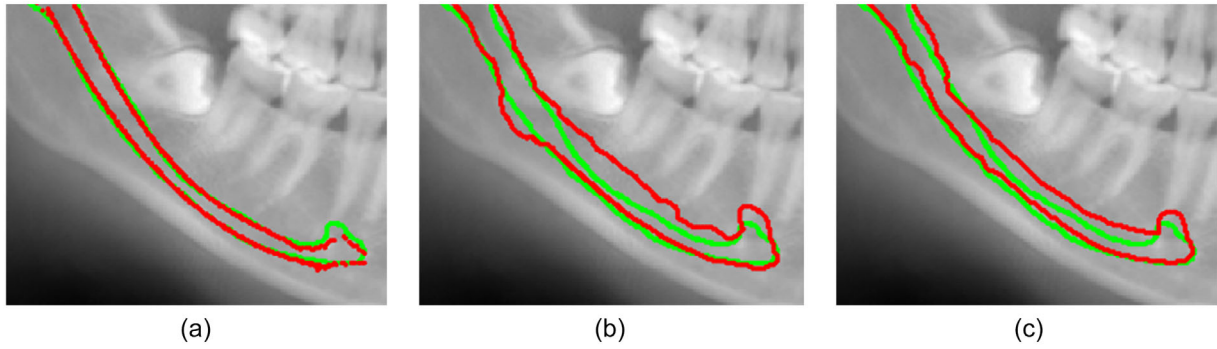


FIGURE 9 Comparison of three segmentation methods. The red IACs are the segmentation result. The green IACs are the doctor segmentation results. (a) The proposed method segmentation result. (b) The 2D U-Net segmentation result. (c) The 3D U-Net segmentation result

certain extent. Therefore, the segmentation results of the proposed method have a higher segmentation accuracy and are closer to the gold standard compared with the other two methods.

3.2 | Quantitative evaluation

In this paper, the dice similarity index (DSI), average symmetric surface distance (ASSD), and mean curve distance (MCD) were selected as the assessment for segmentation results. The definition of the DSI, ASSD, and MCD are given as follow:

$$DSI = \frac{2|A \cap B|}{|A| + |B|} \quad (7)$$

$$ASSD = \frac{1}{|S(A)| + |S(B)|} \times \left[\sum_{a \in S(A)} d(a, S(B)) + \sum_{b \in S(B)} d(b, S(A)) \right] \quad (8)$$

$$MCD = \frac{1}{|C(B)|} \sum_{b \in C(B)} d(b, C(A)) \quad (9)$$

where A is the experimental segmentation result; B is the doctors manual segmentation result; a and b are arbitrary pixels; $S(\cdot)$ is the surface pixel set; $C(\cdot)$ is the curve line point set, the skeletonization result of the segmentation result; $d(\cdot)$ is the shortest distance. The closer the DSI is to 1.00, the smaller the ASSD and MCD, the more accurate the segmentation results.

The DSI, ASSD, and MCD of the left IAC without the fourth-order polynomial are 0.91 (SD = 0.01), 0.21 mm (SD = 0.06 mm), and 1.94 mm (SD = 0.27 mm), respectively; The DSI, ASSD, and MCD of the right IAC without the fourth-order polynomial are 0.92 (SD = 0.02), 0.20 mm (SD = 0.07 mm), and 1.96 mm (SD = 0.32 mm), respectively. Compared with the results of the proposed

method in Table 1, the segmentation accuracy under the fourth-order polynomial fitting is further improved. The specific results of 21 CBCT data segmented based on the proposed method are provided in Appendix B.

Table 1 shows the quantitative comparison results of the four methods. To make a horizontal comparison with Abdolali's method in ref. [12], its reported values were directly quoted. To compare the proposed method and 2D/3D U-Net, the DSI, ASSD, and MCD based on the same 21 cases were recorded in Table 1. The DSI of the proposed method (for both right and left canal) is higher than the 2D and 3D U-Net. The ASSD of the proposed method (for both right and left canal) is lower than that of the other three methods, the MCD of the proposed method (for both right and left canal) is lower than the 2D and 3D U-Net, which shows that our segmentation results are accurate and effective. However, because the rear section of the IAC is distributed at a certain angle with the main canal, there are certain limitations in segmenting the MF from the curved MPR image set. Thus, the MCD of the proposed method is about 1.00 mm higher than the MCD of Abdolali's method in ref. [12].

4 | DISCUSSIONS

In this study, we have shown that the image contrast of the IAC in the curved MPR image set can be enhanced by the gradient direction, the texture features of the GGCM, and the K-means clustering algorithm, which is conducive to segment the edges of the IAC. However, because the rear section of the IAC is distributed at a certain angle with the main canal, the rounded or elliptical MF is gradually distributed in the different layers of the curved MPR image set. Therefore, the segmentation accuracy of the MF is worse than the main canal in the proposed method. Figure 10 shows the distribution of the MF on different layers in a curved MPR image set. The red dashed lines are the central axis of the images, which serves as a reference line to measure the deviation of the MF.

TABLE 1 The performance comparison of IAC segmentation results. The results of the proposed method and 2D/3D U-Net are based on the same 21 cases. Abdolali's method segme are directly quoted.¹²

Method	Left (Mean \pm SD)			Right (Mean \pm SD)		
	DSI	ASSD (mm)	MCD (mm)	DSI	ASSD (mm)	MCD (mm)
The proposed method	0.93 ± 0.01	0.16 ± 0.05	1.59 ± 0.25	0.93 ± 0.02	0.16 ± 0.05	1.60 ± 0.30
Abdolali's method in ref. [12]	—	0.79 ± 0.22	0.92 ± 0.15	—	0.84 ± 0.18	0.82 ± 0.25
2D U-Net	0.67 ± 0.09	1.18 ± 0.97	2.33 ± 0.81	0.68 ± 0.08	1.36 ± 1.18	2.35 ± 0.76
3D U-Net	0.85 ± 0.05	0.54 ± 0.42	2.03 ± 0.88	0.82 ± 0.06	2.07 ± 1.81	1.94 ± 0.54

ASSD, average symmetric surface distance; DSI, dice similarity index; MCD, mean curve distance; SD, standard deviation.

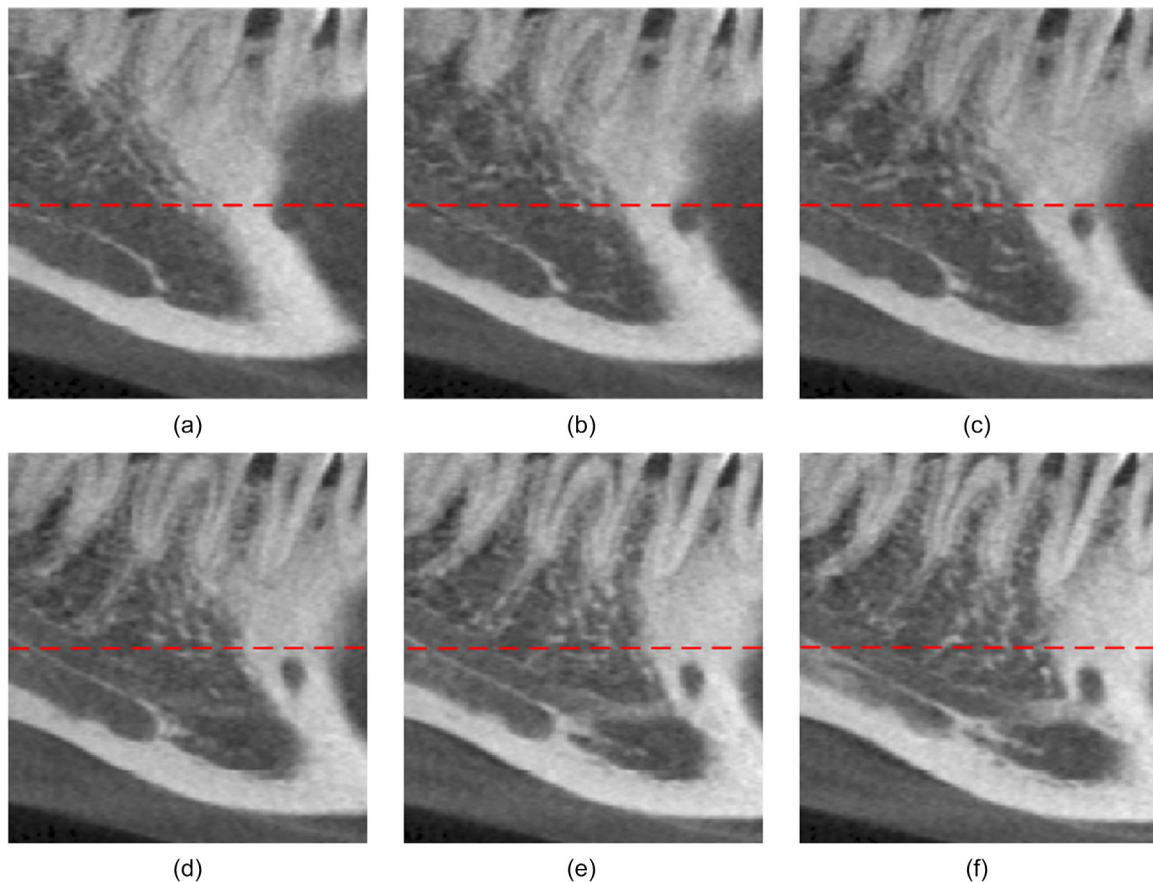


FIGURE 10 Distribution of the MF in a curved MPR image set. The red dashed lines are the central axis of the images. (a–f) The 35th, 37th, 39th, 41st, 43rd, and 45th layers, respectively

To avoid mental nerve and inferior alveolar nerve injury, it is necessary to fully consider the position, number, and size of the MF, the vertical distance between the surgical access line and the IAC before implantation or osteotomy. In the implantation operation, a safety distance of 2.00 mm between the implant and nerve on the coronal aspect of the nerve should be left. In the osteotomy operation, the vertical distance between the surgical access line and the IAC must be at least 2.00 mm. When the distance is less than 1.00 mm, the nerves are easily injured to cause post-operative complications.^{27,28} The proposed method can obtain better segmentation results in the main canal,

which assists the doctor in formulating treatment planning before surgery.²⁹ The segmentation accuracy of the MF is low, and the positioning accuracy of the top of the MF is not enough, which causes certain difficulties in determining the safe area of the MF.

In the curved MPR image set, the MF appears before the main canal. The shape is similar to the circle, and the boundary is clearer on the single-layer curved MPR image (Figure 10). In the segmentation experiment of the 2D and 3D U-Net, we found that the segmentation accuracy of the MF is better than the main canal without blank or black results. In future research, we could further explore the feasibility of deep learning in the

segmentation of anatomical structures with important strategic significance, such as the MF.

The size of the image data has a great influence on the training of the 2D and 3D U-Net. Although the curved MPR image has been divided into left and right parts. All the data were downsampled to reduce the burden on the CPU. However, since the IAC only occupies a small part of the image, the networks were still difficult to give satisfactory segmentation results, and the edges of the mandible were often included in the results. The images had to be preprocessed more finely, and the roughly ROIs of the IAC were used as the input of the network. The panoramas enhanced by the proposed method in this paper can further determine the complete central axis of the IAC due to the better image contrast, which may help to further accurately extract ROIs, and be helpful to the reduction of data volume and the training of the model.

In this paper, 81 CBCT data were used for the experiment of the proposed method and deep learning, which is a relatively small sample. To better train deep learning models, we divided the training set and the test set into 3:1. The proposed method mainly includes image pre-processing, reconstruction, IAC enhancement, and segmentation. The complexity of the steps makes the data processing time longer. In addition, when there are too many artifacts and distortions in the dataset, poor results could be produced. However, deep learning requires less preprocessing and manual operation, which can maximize the use of data for model training. To reduce processing time, computational burden, and compare with 2D/3D U-Net more effectively, we focused on comparing the results of 21 test set data. Combining Figure 8 and Table 1, we found that the performance of the test set is worse than the training set. This is because the model trained on small sample data is prone to overfitting. We also found that, compared to the 2D U-Net, the experimental results of the 3D U-Net are more accurate, but the ASSD and MCD are still higher. In Figure 9, the 3D U-Net shows better possibilities in segmenting the main canal than the 2D U-Net. Therefore, the expansion of experimental data is very important for the training of 2D/3D U-Net, which can improve the accuracy and precision of the model.

The experimental results show that the proposed method can effectively enhance the image contrast of the IAC and further improve the segmentation accuracy. However, when there are excessive metal artifacts, severe mandibular deformities, and adhesion between mandibular tumor and IAC in CBCT data, the segmentation results will have serious edge leakage and incomplete canal. Due to the uncertainty of the IAC travel direction, the segmentation accuracy from the rear section of the IAC to MF is low.^{30,31} In future research, we will explore the location features of the MF, combined with deep learning technology to further improve the segmentation accuracy.

5 | CONCLUSION

To assist the oral clinician to determine the shape and position of the IAC, this paper studied and discussed the IAC segmentation methods based on CBCT images. First, the IAC segmentation methods based on the sagittal images and curved MPR image set are briefly introduced. Then, on the basis of the reconstructed panoramic images with isotropic resolution, an image enhancement method that the K-means clustering algorithm clusters the texture parameters of the GGCM enhanced by the gradient directions is proposed. Finally, the IAC edges are segmented by the 2D line-tracking method, and the tracking results are fitted by the fourth-order polynomial. Experimental results validated that the proposed method can reconstruct a high-contrast curved MPR image set, and accurately segment smooth the IAC edges.

COMPLIANCE WITH ETHICAL STANDARDS

ACKNOWLEDGMENTS

This work was sponsored by [Natural Science Foundation of Shanghai](#) (18ZR1426900), [National Natural Science Foundation of China](#) (61201067). The authors thank Mr. Xuepeng Zhang from the Institute of Medical Imaging & Engineering, University of Shanghai for Science and Technology for the help on deep learning based experiments.

CONFLICT OF INTEREST

The authors declare no conflict of interest.

INFORMED CONSENT

In this article, all data are used with the patient's informed consent.

DATA AVAILABILITY STATEMENT

Research data are not shared.

REFERENCES

1. Balasundaram A, Heir GM, Villegas FP, et al. In vitro correlation of the level of inferior alveolar canal with CBCT imaging. *Surg Radiol Anat.* 2015;37(6):591-597.
2. Kang F, Sah MK, Fei G. Determining the risk relationship associated with inferior alveolar nerve injury following removal of mandibular third molar teeth: a systematic review. *J Stomatol Oral Maxillofac Surg.* 2020;121(1):63-69.
3. Chong BS, Quinn A, Pawar RR, et al. The anatomical relationship between the roots of mandibular second molars and the inferior alveolar nerve. *Int Endod J.* 2015;48(6):549-555.
4. Khorshidi H, Raoofi S, Ghapanchi J, Shahidi S, Paknahad M. Cone beam computed tomographic analysis of the course and position of mandibular canal. *J Maxillofac Oral Surg.* 2017;16(3):306-311.
5. Freire-Maia B, Machado VD, Valerio CS, Custódio ALN, Manzi FR, Junqueira JLC. Evaluation of the accuracy of linear

- measurements on multi-slice and cone beam computed tomography scans to detect the mandibular canal during bilateral sagittal split osteotomy of the mandible. *Int J Oral Maxillofac Surg*. 2017;46(3):296-302.
6. Al-Shayyab MH, Qabba'ah K, Alsoleihat F, Baqain ZH. Age and gender variations in the cone-beam computed tomographic location of mandibular canal: implications for mandibular sagittal split osteotomy. *Med Oral Patol Oral Cir Bucal*. 2019;24(4):e545-e554.
 7. Ludlow JB, Ivanovic M. Comparative dosimetry of dental CBCT devices and 64-slice CT for oral and maxillofacial radiology. *Oral Surg Oral Med Oral Pathol Oral Radiol Endod*. 2008;106(1):106-114.
 8. Tsai CM, Wu FY, Chai JW, Chen MH, Kao CT. The advantage of cone-beam computerized tomography over panoramic radiography and temporomandibular joint quadruple radiography in assessing temporomandibular joint osseous degenerative changes. *J Dent Sci*. 2020;15(2):153-162.
 9. Khaled B, Emad Q, Mohamed P, Shoayeb S. Custom focal trough in cone-beam computed tomography reformatted panoramic versus digital panoramic for mental foramen position to aid implant planning. *J Clin Imaging Sci*. 2020;10:34.
 10. Moris B, Claesen L, Sun Y, Politis C. Automated tracking of the mandibular canal in CBCT images using matching and multiple hypotheses methods. *2012 Fourth International Conference on Communications and Electronics (ICCE)*. CA 90720-1264 USA: IEEE; 2012:327-332.
 11. Lloréns R, Naranjo V, López F, Alcañiz M. Jaw tissues segmentation in dental 3D CT images using fuzzy-connectedness and morphological processing. *Comput Methods Programs Biomed*. 2012;108(2):832-843.
 12. Abdolali F, Zoroofi RA, Abdolali M, Yokota F, Otake Y, Sato Y. Automatic segmentation of mandibular canal in cone beam CT images using conditional statistical shape model and fast marching. *Int J Comput Assist Radiol Surg*. 2017;12(4):581-593.
 13. Abdolali F, Zoroofi RA, Biniiaz A. Fully automated detection of the mandibular canal in cone beam CT images using lie group based statistical shape models. *2018 25th National and 3rd International Iranian Conference on Biomedical Engineering (ICBME)*. NEW YORK, NY 10017 USA: IEEE; 2018:1-6.
 14. Kwak GH, Kwak EJ, Song JM, et al. Automatic mandibular canal detection using a deep convolutional neural network. *Sci Rep*. 2020;10(1):5711.
 15. Jaskari J, Sahlsten J, Järnstedt J, et al. Deep learning method for mandibular canal segmentation in dental cone beam computed tomography volumes. *Sci Rep*. 2020;10(3):5842.
 16. Kondo T, Ong SH, Foong KWC. Computer-based extraction of the inferior alveolar nerve canal in 3-D space. *Comput Methods Programs Biomed*. 2004;76(3):181-191.
 17. Gye Hyun K, Jeongjin L, Ho L, et al. Automatic extraction of inferior alveolar nerve canal using feature-enhancing panoramic volume rendering. *IEEE Trans Biomed Eng*. 2011;58(2):253-264.
 18. Sotthivirat S, Narkbuakaew W. Automatic detection of inferior alveolar nerve canals on CT images. *2006 IEEE Biomedical Circuits and Systems Conference - Healthcare Technology (Bio-Cas)*. NEW YORK, NY 10017 USA: IEEE; 2006:142-145.
 19. Bahrapour E, Zamani A, Kashkouli S, Soltanimehr E, Jahromi MG, Pourshirazi ZS. Accuracy of software designed for automated localization of the inferior alveolar nerve canal on cone beam CT images. *Dentomaxillofac Radiol*. 2016;45(2):20150298.
 20. Kociolok M, Strzelecki M, Obuchowicz R. Does image normalization and intensity resolution impact texture classification. *Comput Med Imag Grap*. 2020;81:101716.
 21. Lam L, Lee SW, Suen CY. Thinning methodologies—a comprehensive survey. *IEEE T Pattern Anal*. 1992;14(9):869-885.
 22. Papakosta TK, Savva AD, Economopoulos TL, et al. An automatic panoramic image reconstruction scheme from dental computed tomography images. *Dentomaxillofac Rad*. 2017;46(4):20160225.
 23. Yun ZQ, Yang S, Huang EL, et al. Automatic reconstruction method for high-contrast panoramic image from dental cone-beam CT data. *Comput Meth Prog Bio*. 2019;175:205-214.
 24. Barone S, Paoli A. CT segmentation of dental shapes by anatomy-driven reformation imaging and B-spline modelling. *Int J Numer Meth Bio*. 2016;32(6):e02747.
 25. Hong JG. Gray level-gradient co-occurrence texture analysis method. *Acta Autom Sin*. 1984;01:22-25.
 26. Chi BW, Yu M, Jiang GY, et al. Blind tone mapped image quality assessment with image segmentation and visual perception. *J Vis Commun Image R*. 2020;67:102752.
 27. Wang XY, Chen KF, Wang S, et al. Relationship between the mental foramen, mandibular canal, and the surgical access line of the mandibular posterior teeth: a cone-beam computed tomographic analysis. *J Endodont*. 2017;43(8):1262-1266.
 28. Greenstein G, Tarnow D. The mental foramen and nerve: clinical and anatomical factors related to dental implant placement: a literature review. *J Periodontol*. 2006;77(12):1933-1943.
 29. San Chong B, Gohil K, Pawar R, et al. Anatomical relationship between mental foramen, mandibular teeth and risk of nerve injury with endodontic treatment. *Clin Oral Invest*. 2017;21(1):381-387.
 30. Nagadia R, Tay ABG, Chan LL, et al. The spatial location of the mandibular canal in Chinese: a CT study. *Int J Oral Maxillofac Surg*. 2011;40(12):1401-1405.
 31. He L, Han SJ. Anatomical position of the mandibular canal in relation to the buccal cortical bone: relevance to sagittal split osteotomy. *J Korean Assoc Oral Maxillofac Surg*. 2018;44(4):167-173.

How to cite this article: Wei X, Wang Y. Inferior alveolar canal segmentation based on cone-beam computed tomography. *Med Phys*. 2021;48:7074–7088.
<https://doi.org/10.1002/mp.15274>

APPENDIX A

Classification and equations of texture features in the ggcm. N_R = normalized maximum gray level ($N_R = 16$ in this paper); N_G = normalized maximum grad level ($N_G = 16$ in this paper); i = gray level; j = grad level; $H(i, j)$ = element of the GGCM; $P(i, j)$ = probability of $H(i, j)$

Feature categories	Feature variables	Formula
Gradient texture features	Small grads dominance	$T_1 = [\sum_{i=1}^{N_R} \sum_{j=1}^{N_G} \frac{H(i,j)}{j^2}] / [\sum_{i=1}^{N_R} \sum_{j=1}^{N_G} H(i,j)]$
	Big grads dominance	$T_2 = [\sum_{i=1}^{N_R} \sum_{j=1}^{N_G} j^2 H(i,j)] / [\sum_{i=1}^{N_R} \sum_{j=1}^{N_G} H(i,j)]$
	Grads asymmetry	$T_3 = \{ \sum_{j=1}^{N_G} [\sum_{i=1}^{N_R} H(i,j)]^2 \} / [\sum_{i=1}^{N_R} \sum_{j=1}^{N_G} H(i,j)]$
	Grads mean	$T_4 = \sum_{j=1}^{N_G} j \cdot [\sum_{i=1}^{N_R} P(i,j)]$
	Grads standard deviation	$T_5 = \{ \sum_{j=1}^{N_G} (j - T_4)^2 [\sum_{i=1}^{N_R} P(i,j)] \}^{\frac{1}{2}}$
	Grads entropy	$T_6 = - \{ \sum_{j=1}^{N_G} [\sum_{i=1}^{N_R} P(i,j)] \cdot \log_2 [\sum_{i=1}^{N_R} P(i,j)] \}$
Gray texture features	Gray asymmetry	$W_1 = \{ \sum_{i=1}^{N_R} [\sum_{j=1}^{N_G} H(i,j)]^2 \} / [\sum_{i=1}^{N_R} \sum_{j=1}^{N_G} H(i,j)]$
	Gray mean	$W_2 = \sum_{i=1}^{N_R} i \cdot [\sum_{j=1}^{N_G} P(i,j)]$
	Gray standard deviation	$W_3 = \{ \sum_{i=1}^{N_R} (i - W_2)^2 [\sum_{j=1}^{N_G} P(i,j)] \}^{\frac{1}{2}}$
	Gray entropy	$W_4 = - \{ \sum_{i=1}^{N_R} [\sum_{j=1}^{N_G} P(i,j)] \cdot \log_2 [\sum_{j=1}^{N_G} P(i,j)] \}$
Hybrid texture features	Energy	$Q_1 = \sum_{i=1}^{N_R} \sum_{j=1}^{N_G} [P(i,j)]^2$
	Correlation	$Q_2 = \frac{1}{T_5 \cdot W_3} \sum_{i=1}^{N_R} \sum_{j=1}^{N_G} (i - W_2)(j - T_4)P(i,j)$
	Hybrid entropy	$Q_3 = - \sum_{i=1}^{N_R} \sum_{j=1}^{N_G} P(i,j) \cdot \log_2 P(i,j)$
	Inertia	$Q_4 = \sum_{i=1}^{N_R} \sum_{j=1}^{N_G} (i - j)^2 P(i,j)$
	Inverse difference moment	$Q_5 = \sum_{i=1}^{N_R} \sum_{j=1}^{N_G} \frac{P(i,j)}{1+(i-j)^2}$

GGCM, gray level-gradient co-occurrence matrix.

APPENDIX B

The results for the DSI, ASSD, and MCD measures are presented for the left and right canals, for the 21 CBCT data

Dataset	Left			Right		
	DSI	ASSD (mm)	MCD (mm)	DSI	ASSD (mm)	MCD (mm)
01	0.92	0.20	2.00	0.94	0.11	1.60
02	0.92	0.17	1.80	0.95	0.09	1.55
03	0.94	0.11	1.33	0.92	0.24	1.75
04	0.91	0.17	1.57	0.92	0.15	1.34
05	0.92	0.22	1.56	0.91	0.17	1.29
06	0.94	0.09	0.89	0.92	0.15	1.40
07	0.94	0.13	1.61	0.93	0.12	1.39
08	0.93	0.13	1.17	0.92	0.17	1.15
09	0.93	0.20	1.68	0.93	0.14	1.40
10	0.94	0.12	1.42	0.94	0.11	1.41
11	0.93	0.26	1.58	0.94	0.24	1.62
12	0.92	0.20	1.84	0.94	0.10	1.42
13	0.95	0.11	2.04	0.93	0.14	1.90
14	0.90	0.23	1.61	0.91	0.22	1.69
15	0.90	0.24	1.60	0.91	0.20	2.14
16	0.93	0.13	1.61	0.91	0.24	2.25
17	0.92	0.19	1.56	0.89	0.28	2.15
18	0.93	0.12	1.75	0.94	0.09	1.29
19	0.92	0.17	1.55	0.92	0.16	1.84
20	0.93	0.14	1.53	0.94	0.11	1.39
21	0.93	0.12	1.60	0.93	0.13	1.71

ASSD, average symmetric surface distance; DSI, dice similarity index; MCD, mean curve distance.

Measure and Evaluate MRgRT 3D Distortion

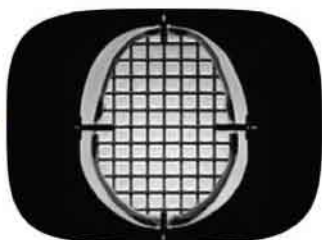


distortioncheck

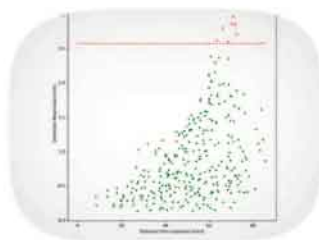
CLOUD SOFTWARE FOR EVALUATION OF IMAGE DISTORTION



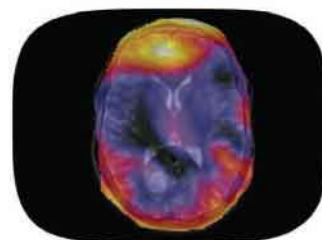
SCAN



**UPLOAD
IMAGES**



**REVIEW REPORTS
& TREND ANALYSIS**



**EXPORT DICOM
OVERLAYS TO TPS**



**Large Field Grid Phantom
2152 Physical Control Points**

- ✓ CIRS proprietary materials simulate distortion due to susceptibility & chemical shifts typical to clinical patient scans
- ✓ Density of physical control points optimized to bring interpolation close to linearity
- ✓ Cloud based solution frees user of operating system and hardware constraints
- ✓ Quickly & automatically analyze complete MR data sets
- ✓ Online deployment facilitates collaboration, easy review and portability of results



**Inter-cranial Grid Phantom
335 Physical Control Points**

CIRS

Tissue Simulation & Phantom Technology

cirsinc.com

900 Asbury Ave., Norfolk, VA 23513, USA • (800) 617-1177